2023 IEEE/ASME International Conference on Advanced Intelligent Mechatronics (AIM)
June 28-30, 2023. Seattle, Washington, USA

Identification and Reduction Method of Normal-Direction Force Ripple in Permanent Magnet Linear Synchronous Motor

Yoon Sik Kwon, Sangmin Lee, and Jun Young Yoon

Abstract— **In this paper, we present identification methods of normal-direction motor parameters and a force ripple reduction method in the normal direction for permanent-magnet linear synchronous motors (PMLSMs). This paper discusses the force generation mechanism of a PMLSM both in the normal and tangential directions by the D- and Q-axis currents, which is utilized for identifying and suppressing the motor force ripple in the normal direction. Using the proposed identification method on the experimental setup of a linear stage driven by an iron-cored PMLSM, we identify the normal-direction force constant with an error of only 7 % as compared to a direct measured data from a dynamometer. The geometry-driven ripple in the normal direction is also identified by experimentally estimating the dominant 2^{nd}- and 6^{th}-order spatial harmonics, which also show significant fidelity with an NRMSE (peak-to-peak normalized root-mean-square error) of only 3.39 % as compared to the dynamometer measurement. Using the identified motor parameters, we achieve the force ripple reduction in the normal direction by 84.6 % and 87.8 % in peak-to-peak and root-mean square (RMS) values, respectively.**

I. Introduction

Permanent-magnet linear synchronous motors (PMLSMs) have been widely utilized in many industries due to their high force density, repeatability, and direct-drive properties [1]–[3]. In order to increase force density of PMLSMs, copper coils are wound around iron-core teeth to concentrate magnetic flux densities [4], [5]. The iron-cored PMLSMs however make the magnetic permeance fluctuate in the airgap region, and therefore undesired force ripples are generated in both moving (tangential) and normal directions [2], [6], which can deteriorate the servo performance and also vibrate the overall systems. A number of studies have been conducted in prior art to identify the force ripples and also to reduce the ripples by shaping multi-phase input currents.

The force ripple is suppressed using a feed-forward compensator, which injects the several current harmonics in [7], [8]. They however utilize the finite element analysis (FEA) to obtain motor parameters such as the force constant and cogging force. Since the FEA-oriented parameters have significant discrepancies with the constructed hardware due to manufacturing errors and magnetic property differences, the ripple reduction performance can be sacrificed. In [9], the detent force is identified using the Fourier curve fitting method by modeling the end- and slot-effect harmonics, which can reduce the calculation time. Such a method however also requires the FEA data in the fitting process. In [10], [11], the cogging force is experimentally identified without an aid of FEA using the fact that the net zero force is applied to a mover in the constant-velocity region. Such approaches allow more accurate cogging identification, thereby suppressing the force ripple more significantly. The aforementioned methods, however, are limited solely to identifying tangential-direction motor parameters.

Most prior studies have focused on identifying motor parameters and reducing force ripples in the tangential direction, not considering the normal-direction force ripples, which can be the main cause of motor system vibrations [12]. Several works have proposed reduction methods of the radial force in rotary motors [13]–[15], however they still utilize the FEA or additional force sensors. As for the normal-direction force ripple in the linear motors, there are less prior studies, and a few research efforts on the normal-direction force ripples in linear motors have been solely by design modifications [2], [6], [16], which cannot be directly applied to commercial motors and constructed motor systems.

We therefore present in this paper the experimental identification methods for normal-direction motor parameters such as the force constant and the geometry-driven ripple, and also a force ripple reduction method in the normal direction. The rest of the paper is organized as follows. Section II shows how motor forces are generated in the normal and tangential directions. In Section III, we present the experimental setup, and Section IV proposes the experimental identification methods for the motor parameters and the ripple reduction method in the normal direction, together with the associated experimental results. We then conclude the paper in Section V.

II. Force Generation Mechanism of PMLSM

We present in this section the force generation mechanism of normal-direction motor force. Fig. 1 shows the three phase-axes (black arrows) of **a**, **b**, and **c**, whose frame is fixed on an armature stator, placed by 120° in electric angle. When the phase currents are applied to such three phase axes, standing electro-magnetic (EM) fluxes are generated on the corresponding axes, which can be commutated to generate a traveling EM flux as depicted with the yellow arrow in the figure. Using the Clarke and Park transformation [17], the traveling EM flux can be divided into the D- and Q-axis EM fluxes, as illustrated with the green and purple arrows in Fig. 1,

This work was supported in part by the National Research Foundation of Korea (NRF) grant funded by the Korea government (MSIT) (No. 2020R1C1C100801311) and partially by Korea Institute for Advancement of Technology (KIAT) grant funded by the Korea government (MOTIE) (P0012744, The Competency Development Program for Industry Specialist).
junyoung.yoon@yonsei.ac.kr

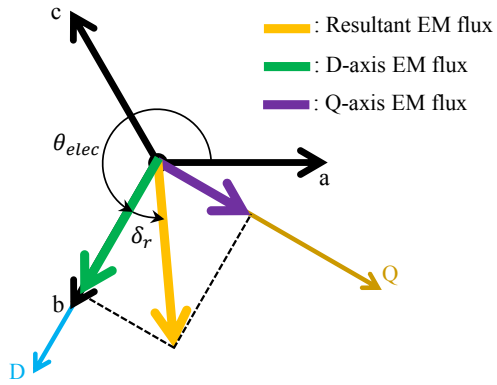

Fig. 1. EM fluxes on space vector plane. Regulating three phase currents can generate the traveling EM flux, which can be divided into D-Q axes.

respectively. Note that the D-Q axes, fixed on the moving PM track, rotates with the electric angle θ_{elec} in the space vector plane, which is corresponding to the PM mover displacement in the tangential direction as shown in Fig. 2.

Fig. 2 represents the iron-cored PMLSM schematic where each axis of **a**, **b**, and **c** is fixed on the corresponding iron-cored tooth while the D-Q axes are moving along the PM mover. The D-axis is aligned with an upward-magnetized PM and the Q-axis is located at the center of alternately-magnetized PMs, leading the D-axis by 90° in electric angle. The PM mover displacement is defined from the **a**-axis, which can be converted to an electric angle θ_{elec} via the pole-pair pitch λ_{pp}, as illustrated in Fig. 2. When we regulate the three-phase currents to locate the resultant EM flux on the D-axis, as shown in the left magnified view in the figure, it generates the normal-direction Lorentz force. Note that the D-axis EM flux can both attract and repel the PM mover according to the D-axis EM flux direction.

We can also locate the resultant EM flux on Q-axis, as illustrated in the right magnified view. Since the Q-axis EM flux (purple arrow) pulls and repels the adjacent PMs in the same magnitude, the normal components of Lorentz forces (dotted arrows) are nominally canceled out while the tangential components are added in the same direction, thereby generating solely the tangential-direction Lorentz force. The Q-axis current can also generate the tangential-direction force both in the forward and backward depending on the Q-axis EM flux direction. Note that the effects of the D- and Q-axis EM fluxes can be superposed under the assumption of unsaturated materials. Using the aforementioned force generation mechanism, we can generate both the normal- and tangential-direction motor forces in PMLSMs, and can therefore reduce the normal-direction force ripples using the identified motor parameters discussed in Section IV.

III. Experimental Setup

Fig. 3 shows the experimental linear stage setup utilized to validate the identification method of normal-direction motor parameters and the force ripple reduction method in the normal

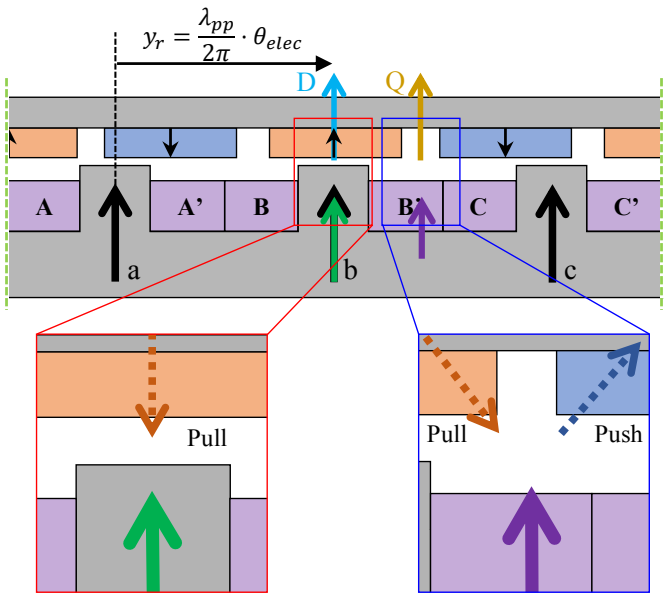

Fig. 2. D-Q representation on iron-cored PMLSM. The D-axis is aligned with an upward-magnetized PM and the Q-axis leads the D-axis by 90° in electric angle. When locating EM flux on the D-axis, the normal-direction Lorentz force is generated, attracting or repelling the PM mover (left magnified figure). When locating EM flux on the Q-axis, on the other hand, the tangential-direction Lorentz force is generated by pulling and pushing the adjacent PMs (right magnified figure).

TABLE I
PMLSM Dimension

Description	Value
Width of PM	30 mm
Height of PM	2.5 mm
Pole-pair pitch (λ_{pp})	75 mm
Width of iron-core tooth	16 mm
Width of armature yoke	300 mm
Depth of motor (D)	75 mm

direction, discussed in Section IV. The PM mover with a pole-pair pitch λ_{pp} of 75 mm is installed underneath the moving stage, and the iron-cored armature stator is fixed on the dynamometer (Type 9129 AA by Kistler) in order to directly measure the motor forces in the normal and tangential directions as shown in Fig. 3a. The associated motor parameters are organized in Table I. Note that the dynamometer is not utilized in the proposed identification methods. It is used solely for the purpose of the validation of the proposed identification methods and the force ripple reduction performance. The mover position is measured by the optical encoder (interface TI0020A08A and read-head T1031 by Renishaw), whose output quadrature signal is transferred to the FPGA module (PXIe-7856R by National Instrument). The position data is then transmitted to the real-time controller (PXIe-8861 by NI), shown in Fig. 3b, running the position-control loop at 10 kHz with a -3 dB bandwidth of 100 Hz. We utilize the motor amplifier (B30A40 by Advanced Motion Control) to drive three-phase currents to armature coils, and

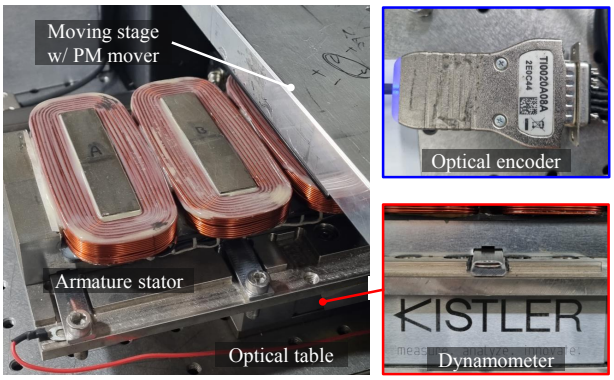

(a)

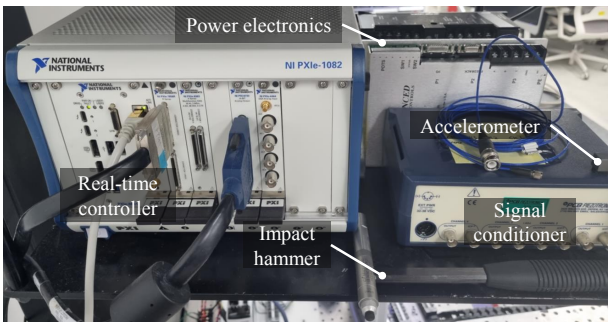

(b)

Fig. 3. Experimental setup of a linear stage, real-time controller, and associated electronics. (a) The linear stage is driven by an iron-cored PMLSM. The mover position is determined by an optical encoder and the motor force is measured by a dynamomter installed under the armature stator. (b) Real-time controller with FPGA is utilized to control the motor and receive sensor signals from an accelerometer and an impact hammer. The command signal from control loop is sent to power electronics so as to excite the armature coils.

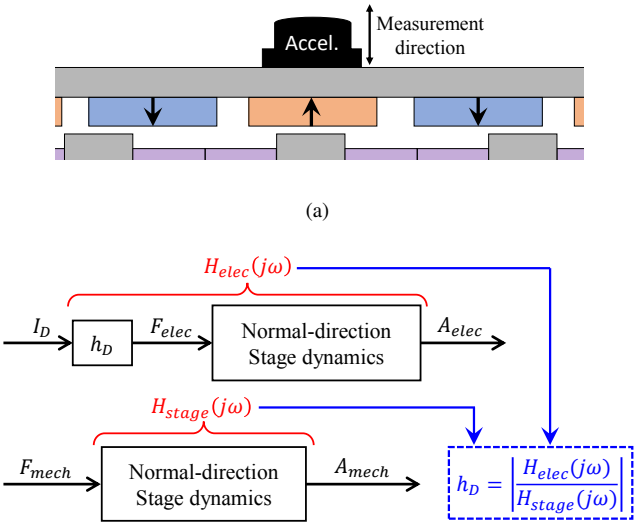

(a)

(b)

Fig. 4. Schematic diagram for identification of normal-direction force constant h_D. When exciting the PM mover in the normal direction b y the D-axis current I_D and by the mechanical impact force, the system responses of H_{elec} and H_{stage} are obtained, respectively. (a) The responses are measured by the accelerometer mounted on the PM mover. (b) Since H_{elec} consists of the normal-direction force constant h_D and the stage dynamics H_{stage}, h_D can be obtained by dividing H_{elec} by H_{stage}.

the high bus voltage is supplied by the DC power supply (PS30A by AMC). An impact hammer and an accelerometer charged by a signal conditioner (086C03, 330B40, and 482C24 by PCB Piezotronics, respectively) are used to identify the normal-direction force constant h_D and the geometry-driven ripple $F_{GDR,n}$, as presented in Section IV.

IV. Identification Method for Normal-Direction Motor Parameters and Ripple Reduction Method

In this section, we present the experimental identification method for the normal-direction motor parameters such as i) the force constant h_D and ii) the geometry-driven ripple $F_{GDR,n}$, representing the cogging force between the PMs and the iron-core teeth, which are utilized for the ripple reduction method in Section IV-C. We also show in this section the corresponding experimental results on the motor force parameter identification and the normal-direction ripple reduction.

A. Normal-direction force constant

Using the stage dynamics H_{stage}, we can identify the normal-direction force constant h_D. Fig. 4 illustrates the overall process of such identification method. An accelerometer is installed on the PM mover, as shown in Fig. 4a, to directly measure the normal-direction acceleration capturing the stage dynamics. When the D-axis current is applied to the PMLSM, the normal-direction Lorentz force is generated as discussed in Section II, exciting the stage dynamics in the normal direction. Such an electrically-excited system response H_{elec} can be measured by sweeping the D-axis current excitation for a range of frequencies. Note that H_{elec} consists of the normal-direction force constant h_D and the stage dynamics, as depicted in Fig. 4b. We can also excite solely the stage dynamics H_{stage} by mechanically hitting the stage with an impact hammer. We can then obtain the normal-direction force constant h_D by dividing H_{elec} by H_{stage}, written as

$$h_D = \left| \frac{H_{elec}(j\omega)}{H_{stage}(j\omega)} \right|. \tag{1}$$

Fig. 5 shows the experimentally measured frequency responses of H_{elec} and H_{stage}, shown with the black and purple curves, respectively. Using (1) and the measured experimental data in Fig. 5, the normal-direction force constant h_D can be obtained as 305 N/A. This shows a small error of 7 % as compared to the measured normal-direction force constant of 327 N/A directly obtained by the dynamometer. Note that we choose the stage bending mode frequency f_{mover} of 346.8 Hz when obtaining the h_D. This is because the responses in the relatively low frequency range, namely below 250 Hz, show a bit of discrepancy due to the force action point difference between the mechanical and electrical excitations.

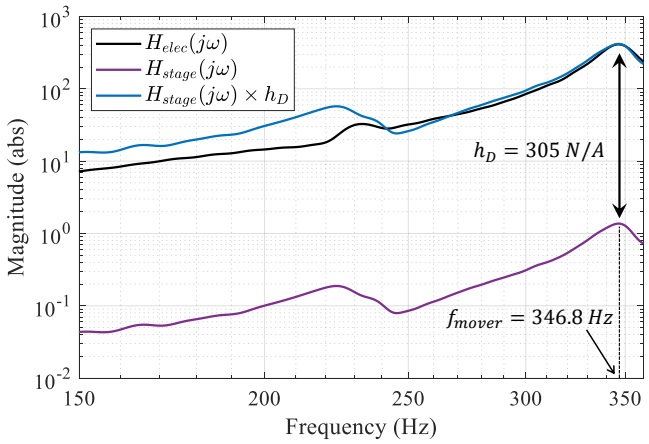

Fig. 5. Measured frequency responses H_{elec} (black curve) and H_{stage} (purple curve). Dividing H_{elec} by H_{stage} at the mode frequency of 346.8 Hz, the normal-direction force constant h_D is obtained as 305 N/A.

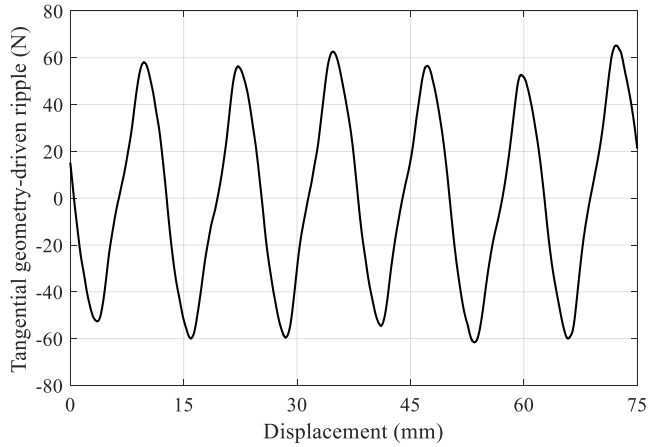

Fig. 6. Identified tangential-direction geometry-driven ripple $F_{GDR,t}$ in our previous study [10].

B. Geometry-driven ripple in normal direction

Since the iron-cored PMLSM has a periodic configuration of 3-phase-4-magnets as depicted in Fig. 2, the geometry-driven ripple $F_{GDR,n}$ consists of several dominant spatial harmonics, expressed as

$$F_{GDR,n} = \sum_k F_k \cos\left(\frac{2\pi}{\lambda_k} + \phi_k\right) \tag{2}$$

where F_k, λ_k, and ϕ_k are the force amplitude, spatial period, and spatial phase of associated spatial harmonics, respectively. We can identify the geometry-driven ripple in the normal direction $F_{GDR,n}$ by obtaining such parameters. The PMLSM setup used in this paper is an iron-cored type and has a configuration of a long PM mover and short armature stator modules, and there exist the end and slotting effects, causing 2nd- and 6th-order spatial harmonics. We therefore focus on these two harmonic numbers k of 2 and 6 in order to identify $F_{GDR,n}$ in (2).

We can first obtain the spatial phases ϕ_k of $F_{GDR,n}$ by

TABLE II

IDENTIFIED AND MEASURED SPATIAL HARMONICS OF $F_{GDR,n}$

	Spatial phase (°)		Amplitude (N)	
Harmonic	2nd	6th	2nd	6th
Identified	51.1	169.2	33.3	107.8
Measured	64.5	166.8	37.7	105.3
Error (%)	13.4	2.4	11.6	2.4

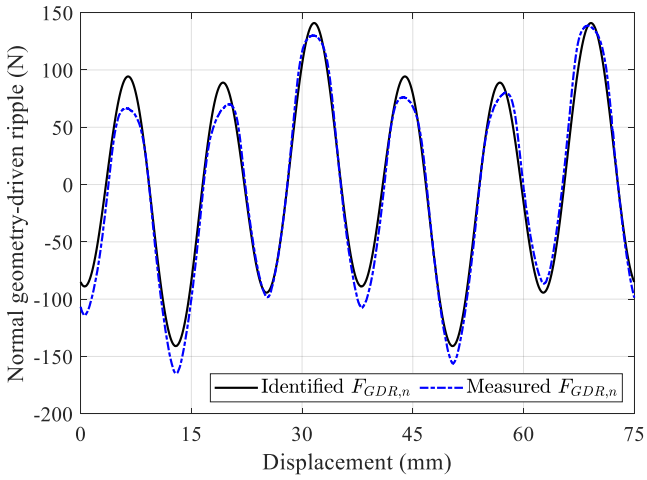

Fig. 7. Identified normal-direction geometry-driven ripple $F_{GDR,n}$, showing a small NRMSE of 3.39 % as compared to the measured ripple data by dynanomter.

shifting the spatial phases of the geometry-driven ripples in the tangential direction $F_{GDR,t}$ by 90° in electric angle. Note that $F_{GDR,t}$ is experimentally identified in our previous study [10]. Using the identified $F_{GDR,t}$ in Fig. 6, the spatial phases of $F_{GDR,n}$ are calculated and organized in Table II. The identified spatial phases of 2nd- and 6th-order harmonic are 51.1° and 169.2°, respectively, showing small errors of 13.4 % and 2.4 % as compared to the measured data by the dynamometer.

When we move the stage at a velocity of v_{stage}, the normal-direction geometry-driven ripple $F_{GDR,n}$ vibrates the stage at a frequency ω_k of

$$\omega_k = 2\pi \frac{v_{stage}}{\lambda_k}. \tag{3}$$

Utilizing the relation between A_{elec} and F_{elec} shown in Fig. 4, written as

$$\left|\frac{A_{elec}(j\omega)}{F_{elec}(j\omega)}\right| = \frac{|H_{elec}(jw)|}{h_D} \tag{4}$$

and also using (3), we can identify the force amplitude F_k as

$$F_k = F_{elec}(j\omega)|_{\omega=\omega_k} = h_D \left|\frac{A_{elec}(j\omega)}{H_{elec}(j\omega)}\right|_{\omega=\omega_k}. \tag{5}$$

In our experimental setup, the 2nd- and 6th-order spatial periods are $\lambda_2 = 37.5$ mm and $\lambda_6 = 12.5$ mm, respectively. The moving stage is commanded to move at a velocity v_{stage} of 3.0 m/s, exciting the moving stage at the frequencies of 80 Hz

TABLE III
FORCE RIPPLE REDUCTION IN THE NORMAL DIRECTION

	Uncompensated (N)	Compensated (N)	Reduction rate (%)
peak-to-peak	294.3	45.4	84.6
RMS value	80.7	9.8	87.8

and 240 Hz for the 2nd- and 6th-order harmonics, respectively. The stage vibration accelerations are measured at such frequencies as $A_{elec}(j\omega_2) = 0.25$ m/s^2 and $A_{elec}(j\omega_6) = 10.15$ m/s^2. We can then identify the force amplitudes of the 2nd- and 6th-order harmonics using (5), as $F_2 = 33.3$ N and $F_6 = 107.8$ N, respectively. As compared to the measured force amplitudes by the daynamomter, the errors are as small as 11.6 % and 2.4 %, respectively, as also organized in Table II. The geometry-driven ripple $F_{GDR,n}$ is then calculated by (2) as shown in Fig. 7, showing high fidelity with a small NRMSE (peak-to-peak normalized root-mean-square error) of 3.39 % as compared to the measured $F_{GDR,n}$ by the dynamomter. Using the identified h_D and $F_{GDR,n}$, the force ripple reduction method in the normal direction and the associated experimental data are presented in the following subsection.

C. Ripple reduction of force ripple in normal direction

The force equations of surface-mounted PMLSM in tangential and normal directions can be written as

$$\begin{aligned} F_t(y_r, I_Q) &= F_{GDR,t}(y_r) + k_f I_Q \\ F_n(y_r, I_D) &= F_{GDR,n}(y_r) + h_D I_D \end{aligned} \tag{6}$$

where k_f is the force constant in tangential direction. Note that the reluctance force in normal direction is neglected due to its relatively small magnitude, and the reluctance force in tangential direction has zero value for surface-mounted PMLSM. The force ripple reduction method can be derived from this decoupled force equation.

The normal-direction force ripple can be reduced by compensating the D-axis current, using the identified normal-direction motor parameters of h_D and $F_{GDR,n}$, as

$$I_{D,comp}(y_r) = -\frac{F_{GDR,n}(y_r)}{h_D}. \tag{7}$$

The minus sign represents that the generated Lorentz force by $I_{D,comp}$ cancels out the normal-direction geometry-driven ripple $F_{GDR,n}$. Fig. 8 shows the experimental result of force ripple reduction in the normal direction when the stage is commanded to move at a constant velocity. The force ripple is significantly reduced by 84.6 % in peak-to-peak from 294.3 N to 45.4 N, and 87.8 % in root-mean-square (RMS) value from 80.7 N to 9.8 N, respectively, which are also organized in Table III.

Note that we assume in this paper that the normal- and tangential-direction motor forces are nominally decoupled by the D- and Q-axis currents, respectively, as presented in Section II and (IV-C). The Q-axis current, however, also generates the normal-direction motor force by attracting the back-iron of the PM mover, which is neglected in this paper, and thereby the ripple reduction method in (7) is limited to only a constant-velocity region or near-zero region of the Q-axis current. In order to overcome such difficulties, we are currently working as future research on the identification methods for the additional normal-direction motor parameters, such as the normal-direction force constant by the Q-axis current and the position-dependent force constants, so as to enhance the force ripple reduction performance.

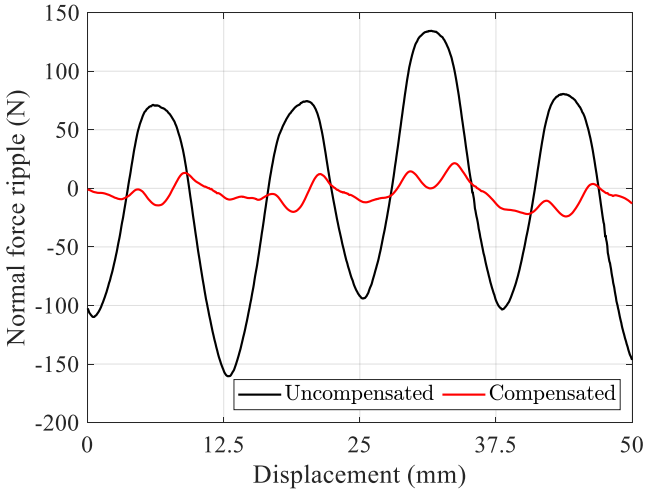

Fig. 8. Experimental result of force ripple reduction in the normal direction. As compared to the uncompensated case, the normal-direction force ripple is significantly reduced by 84.6 % and 87.8 % in peak to peak and RMS value, respectively.

V. CONCLUSION

We in this paper present the identification method of the normal-direction motor parameters and also the reduction method of the normal-direction force ripple in permanent-magnet linear synchronous motors (PMLSMs). The force generation mechanism of PMLSMs is discussed using the D-Q axes on the PMLSM configuration, presenting how the motor forces are generated in both normal and tangential directions. Using the proposed identification methods, we successfully identify the motor parameters such as the normal-direction force constant and the geometry-driven ripple with a small error of 7 % and a small NRMSE 3.39 %, respectively, as compared to the direct measurement data by the dynamometer. We also achieve a significant force ripple redection in the normal direction using the identified motor parameters, showing the reduction rate of 84.6 % and 87.8 % in peak-to-peak and root-mean-square (RMS) value, respectively. We are currently researching as a future work on the simultaneous ripple reduction both in the normal and tangential directions, which can also be applied in acceleration regions of moving stages.

REFERENCES

[1] J. H. Kim, S. W. Jung, Y. S. Kwon, S. Lee, and J. Y. Yoon, "Modeling of current-driven end-effect force ripple in air-cored linear synchronous

motor with multiple modular stators," *IEEE Transactions on Industrial Electronics*, pp. 1–9, 2022.

[2] J. Y. Yoon, L. Zhou, and D. L. Trumper, "Linear stages for next generation precision motion systems," in *2019 IEEE/ASME International Conference on Advanced Intelligent Mechatronics (AIM)*. IEEE, 2019, pp. 241–247.

[3] D. Fu, K. Wu, P. Zheng, Q. Yu, and X. Wu, "Force modeling and analysis of a tube flux-switching transverse-flux permanent magnet linear motor," *IEEE Transactions on Industry Applications*, vol. 58, no. 4, pp. 4575–4586, 2022.

[4] E. K. Kim, W. Song, Y. S. Kwon, J. H. Kim, H. M. Yoon, H. G. Lee, and J. Y. Yoon, "Vibration-generation mechanism and reduction method in linear iron-cored permanent-magnet synchronous motors at stationary state," *IEEE/ASME Transactions on Mechatronics*, 2022.

[5] X. Zhao, Y. Du, R. Zhang, K. Guo, and H. Wang, "Comparative research on performance of iron-core and ironless permanent magnetic linear synchronous motor," in *2022 25th International Conference on Electrical Machines and Systems (ICEMS)*. IEEE, 2022, pp. 1–5.

[6] J. Y. Yoon, J. H. Lang, and D. L. Trumper, "Double-sided linear iron-core fine-tooth motor for low acoustic noise and high acceleration," *IEEE/ASME Transactions on Mechatronics*, vol. 24, no. 5, pp. 2161–2170, 2019.

[7] Z. Chen, W. Kong, Y. Zhou, R. Qu, and V. Fedida, "Thrust force ripple reduction of h-lvpmm based on dynamic harmonic current compensation," *IET Electric Power Applications*, vol. 14, no. 2, pp. 226–233, 2020.

[8] Hongyun Jia, M. Cheng, W. Hua, Zhengzhuan Yang, and Yunqian Zhang, "Compensation of cogging torque for flux-switching permanent magnet motor based on current harmonics injection," in *2009 IEEE International Electric Machines and Drives Conference*, 2009, pp. 286–291.

[9] Y. Zhu, S. Jin, K. Chung, and Y. Cho, "Control-based reduction of detent force for permanent magnet linear synchronous motor," *IEEE Transactions on Magnetics*, vol. 45, no. 6, pp. 2827–2830, 2009.

[10] Y. S. Kwon, S. Lee, and J. Y. Yoon, "Force ripple reduction in permanent magnet linear synchronous motor with position-dependent force constant identification," in *2022 IEEE/ASME International Conference on Advanced Intelligent Mechatronics (AIM)*. IEEE, 2022, pp. 1355–1359.

[11] L. Bascetta, P. Rocco, and G. Magnani, "Force ripple compensation in linear motors based on closed-loop position-dependent identification," *IEEE/ASME Transactions on Mechatronics*, vol. 15, no. 3, pp. 349–359, 2009.

[12] M. Tsypkin, "The origin of the electromagnetic vibration of induction motors operating in modern industry: Practical experience-analysis and diagnostics," *IEEE Transactions on Industry Applications*, vol. 53, no. 2, pp. 1669–1676, 2016.

[13] M. Kawa, K. Kiyota, J. Furqani, and A. Chiba, "Acoustic noise reduction of a high-efficiency switched reluctance motor for hybrid electric vehicles with novel current waveform," *IEEE Transactions on Industry Applications*, vol. 55, no. 3, pp. 2519–2528, 2018.

[14] F.-C. Lin and S.-M. Yang, "An approach to producing controlled radial force in a switched reluctance motor," *IEEE Transactions on Industrial Electronics*, vol. 54, no. 4, pp. 2137–2146, 2007.

[15] A. Chiba, M. A. Rahman, and T. Fukao, "Radial force in a bearingless reluctance motor," *IEEE transactions on magnetics*, vol. 27, no. 2, pp. 786–790, 1991.

[16] X. Huang, T. Ji, L. Li, B. Zhou, Z. Zhang, D. Gerada, and C. Gerada, "Detent force, thrust, and normal force of the short-primary double-sided permanent magnet linear synchronous motor with slot-shift structure," *IEEE Transactions on Energy Conversion*, vol. 34, no. 3, pp. 1411–1421, 2019.

[17] J. R. Mevey, "Sensorless field oriented control of brushless permanent magnet synchronous motors," Master's thesis, Kansas State University, 2009.